Simulations of lateral mixing in cross-channel flow

J.J. Derksen

Chemical & Materials Engineering Department, University of Alberta, Edmonton, Alberta, Canada T6G 2G6

ARTICLE INFO

ABSTRACT

Cross flow phenomena between connected sub-channels are studied by means of numerical simulations based on lattice-Boltzmann discretization. The cross (that is lateral) transfer is largely due to macroscopic instabilities developing at two shear layers. The characteristic size and advection velocity of the instabilities favorably compare with experimental results from the literature on a geometrically similar system. The strength of the cross flow strongly depends on the Reynolds number, with cross flow developing only for Reynolds numbers (based on macroscopic flow quantities) larger than 1360. Mass transfer between the sub-channels has been assessed by adding a passive scalar to the flow and solving its transport equation. As a result of the intimate connection of cross flow and lateral mass transfer, also the mass transfer coefficient is a pronounced function of Re.

1. Introduction

Flow phenomena as occurring in the interstitial space in tube bundles in (nuclear) heat exchangers are relevant for the heat transfer performance and mechanical stability of the equipment [1,2]. The stability relates to forces induced by the large-scale and often coherent flow structures that develop in such systems. In case the main flow direction and the tube centerlines are perpendicular, complex vortex shedding patterns occur that strongly depend on the arrangement of the tubes in the bundle [3]. In this paper, however, the situation where tube centerlines and main flow direction are essentially parallel is considered. In that situation large-scale flow structures develop at the free shear layers that divide parts of the channels with different cross-sectional area [4]. These structures induce strong secondary flows (termed cross flows in this paper) perpendicular to the (primary) streamwise direction. In addition to their practical relevance for heat exchanging equipment, the cross flow instabilities exhibit interesting fluid mechanics as they show an intriguing transition from stable laminar, via unstable laminar to turbulent flow with (as indicated above) the development of large-scale structures and transverse transport.

As for essentially all transitional flows with coherent fluctuations, their modeling is intricate. Since the turbulence is not fully developed, and part of the fluctuations behave (semi) deterministically, conditions for (conventional) turbulence closure are not met. On the other hand, direct numerical simulations, i.e. simulations that solve the Navier–Stokes equations without inferring a turbulence model, require significant computational resources

since the flow needs to be resolved down to its smallest scales. In this paper, we explore the applicability and feasibility of direct simulations of cross flow in a broad range of Reynolds numbers (up to $Re_s = O(10^4)$, with the Re_s based on macroscopic flow quantities, see its definition below) facilitated by parallel processing and an efficient numerical scheme. For its inherently parallel nature, and its efficiency not being hampered by geometrical complexity we use the lattice-Boltzmann method for solving the Navier–Stokes equations. We assess – specifically for the high end of the Reynolds number range – the effects of spatial resolution on the numerical results. Since (from the application side) heat transfer is an essential feature in tube bundles, we study the contribution of cross flow to the lateral spreading of a passive scalar. The convection–diffusion equation for the passive scalar is solved by means of an explicit finite volume formulation with specific attention for controlling numerical diffusion.

The aim of this paper is to resolve and visualize the instabilities in a typical cross flow geometry at a range of Reynolds numbers covering transitional flow; and to quantify to what extent cross flow contributes to lateral scalar mixing. The results, at least those at the higher Reynolds numbers considered here, also can act as a benchmark for the performance of turbulence models applied to the same flow system. The use of turbulence models becomes inevitable when simulating cross flows at the much higher Reynolds numbers characteristic for (nuclear) industrial applications. Finally the paper is a demonstration of the lattice-Boltzmann method coupled to a finite volume scalar transport solver as an efficient tool for simulations of transitional and turbulent flows.

The geometry and flow analysis as used here is inspired by the experimental work due to Lexmond et al. [5] (2005), see Fig. 1.

E-mail address: jos@ualberta.ca

They reported particle image velocimetry (PIV) experiments in a cross flow setup, where they quantified the occurrence of coherent flow structures in terms of their size and the velocity with which they were advected. Their results are used here as a means of experimental validation, specifically in view of the simplifying assumptions in terms of boundary conditions that were made to help the feasibility of our simulations: Periodic conditions in the streamwise direction were used in most of the simulations to save on the computational effort related to entrance effects. As in the experimental work, this paper will consider single phase, incompressible, isothermal flow. In addition to the experiments the simulations consider the transport of a passive scalar.

This paper starts with a brief account of the flow geometry, and the flow conditions including a summary of the experimental observations of Lexmond et al. [5]. In the subsequent section the numerical procedures for flow and scalar transport modeling are described, and the parallelization strategy is outlined. In discussing the results, we first show impressions of the flow structures that were resolved. Then we perform a number of verifications, including grid resolution tests and spectral analysis to assess the level with which turbulence is being resolved. Subsequently the onset of macroscopic instabilities and their dependence on the Reynolds number will be presented and related to the experimental data. Then scalar transport results will be discussed and lateral mixing will be quantified. The final section summarizes and draws conclusions.

2. Definition of the flow

Fig. 1 shows the flow geometry, and the coordinate system that will be used throughout this paper. It is a straight channel with uniform cross section consisting of two larger rectangular portions (sub-channels) connected through a narrow slit. The primary flow is in the positive x-direction. The cross section is left–right symmetric. In most of the simulations presented here, we will consider periodic boundary conditions in the streamwise direction. In these cases the flow is driven by a uniform body force f_0 in the positive x-direction that represents an average pressure gradient: $f_0 = -\frac{d\langle p \rangle}{dx}$. In one case the flow in the channel is due to an inflow in the x-direction, uniformly distributed over the cross-sectional area. In that case the outflow has a zero-gradient boundary condition.

At the shear planes (which are the xz-planes at $y = \pm\frac{W}{2}$ that separate the wide and narrow parts of the cross section) instabilities develop, akin to the ones observed at a free shear layer as e.g. described in the seminal paper by Brown and Roshko [6], a major dif-
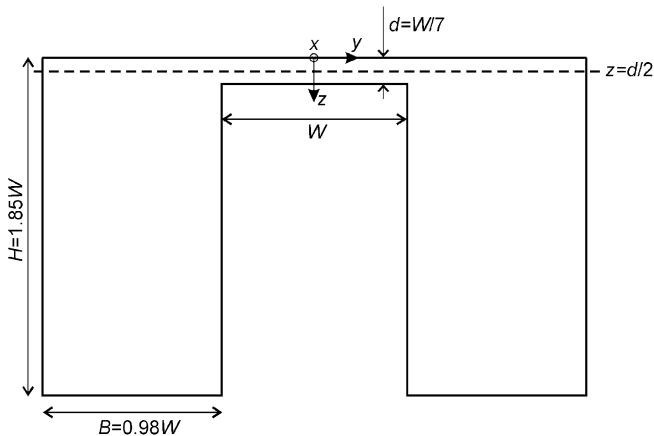
ference being the close proximity of the top wall. Free shear layers have been investigated in great detail by numerous authors, e.g. see the review by Ho and Huerre [7], and [8–12] for more recent advancements in the field. A schematic of the instabilities occurring in the specific geometry being studied here (as inspired by the experimental work [5]) along with the definition of their characteristic dimension S is given in Fig. 2. In line with the experimental work, a macroscopic Reynolds number (that fully defines this single phase, isothermal flow) is based on the hydraulic diameter of the channel ($D_h = \frac{4V}{A}$, with V the total volume of the channel, and A the total wall surface area), and on the superficial velocity $u_s \equiv \frac{\phi_V}{A_{crss}}$ (with ϕ_V the volumetric flow rate, and A_{crss} the cross-sectional area of the channel): $\mathrm{Re}_s = \frac{u_s D_h}{\nu}$. Given the geometrical layout (Fig. 1) $D_h = 1.157W = 8.097d$ with d the height of the slit connecting the two sub-channels. As a result, a Reynolds number based on the flow in the slit (length scale d, average velocity in the slit significantly smaller than u_s) would be typically one order of magnitude lower than Re_s.

It should be noted that in the simulations with periodic boundary conditions Re_s cannot be set a priori. In steady state the (eventual) superficial velocity is the result of a force balance in x-direction on the entire fluid volume: $f_0 V = \langle\tau_w\rangle A$ with $\langle\tau_w\rangle$ the average wall shear stress. For a priori characterizing the flow we therefore have a second Reynolds number Re_w that is based on

Fig. 1. Cross section through the channel which consists of two rectangular subchannels connected though a slit with height d, and definition of the coordinate system. The dashed line indicates the primary plane of observation.
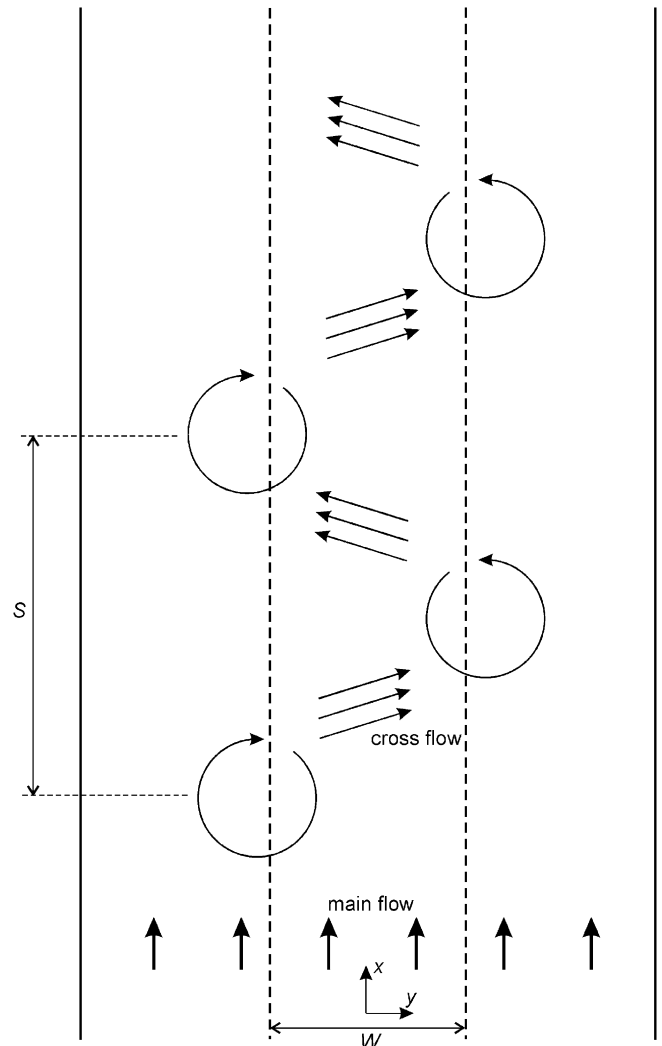

Fig. 2. Schematic view of cross flow in an xy-plane through the slit with a definition of the structure size S.

the wall shear velocity related to the average wall shear stress $u_w = \sqrt{\frac{\langle \tau_w \rangle}{\rho}}$: $Re_w = \frac{u_w D_h}{\nu}$.

Fig. 2 is a schematic of the experimentally observed flow structures. At the shear layers instabilities develop that transport liquid from left to right and vice versa. These secondary flow structures are transported downstream with a well-defined speed (the structure velocity u_{struct}). In the experiments this speed is determined by cross correlating time series of the transverse (y) velocity in two monitor points in the center of the slit at a mutual distance Δx in x-direction. The two signals are to some extent periodic and have a delay time (determined from the cross correlation) τ_d so that $u_{struct} = \frac{\Delta x}{\tau_d}$. The structure size S (see Fig. 2) follows from the frequency (f) of the velocity time series and the structure velocity: $S = \frac{u_{struct}}{f}$. The largest uncertainty in this analysis is the determination of the frequency given the phase jumps and other non-periodic effects in the velocity time series. Among other results, Ref. [5] reports structure velocity ratios $\frac{u_{struct}}{u_s}$ and size ratios $\frac{S}{D_h}$ as a function of the macroscopic Reynolds number Re_s. The experimental observations are mainly made in the xy-plane at $z = \frac{d}{2}$; this plane is indicated by the dashed line in Fig. 1.

Clearly the periodic boundary conditions in streamwise direction as used in the simulations need to be considered with great care. If the domain size in x-direction (L) is taken too small in relation to S, the flow will not develop instabilities at all, or will organize itself such that $S = L$. Therefore L should be taken significantly larger than the expected size of the structures. Still, in the periodic domain the structure size will be quantized ($mS = L$, with m an integer number). To relate the computational and experimental results the sensitivity of S with respect to the choice of L has been considered. In addition, also the simulation with non-periodic streamwise boundary conditions has been used to check structure sizes, and the distance required to fully develop unstable, periodic flow.

3. Modeling set up

The lattice-Boltzmann method [13,14] has been used for simulating the fluid flow. It is a particle-based method with excellent scaling properties on parallel computer platforms, and with a computational efficiency not being hampered by geometrical complexity. The specific scheme employed here is due to Somers [15], see also [16]. It is a variant of the widely used lattice BGK schemes (see e.g. [17]). The way it deals with higher-order terms gives it enhanced stability at low viscosities which makes it well suited for turbulence simulations [18–20]. No turbulence model has been applied, i.e. the lattice-Boltzmann method was used to directly solve the Navier–Stokes equations.

Our implementation of the lattice-Boltzmann scheme makes use of a uniform, cubic grid. In order to sufficiently resolve the flow, it was considered essential to accurately capture the z-gradients in the slit. For this we took 15 spacings in the z-direction there ($\Delta = \frac{d}{15}$), and checked the sensitivity of this choice for one specific flow case by also performing simulations at $\Delta = \frac{d}{20}$ and $\Delta = \frac{d}{10}$. The use of a uniform, cubic grid implied that the linear dimensions B and H (see Fig. 1) of the two sub-channels slightly changed (by 1/3 of a grid spacing, i.e. less than 0.5% of B) when changing the spatial resolution. The aspect ratio $\frac{W}{d}$ of the slit did not change from one grid to the other.

Given the geometry only consisting of plane walls, the halfway bounce-back rule (e.g. [14]) can be employed to achieve the no-slip condition. As noted above, the entrance and exit planes ($x = 0$, and $x = L$) are either periodic, or have an imposed, uniform velocity and a $\frac{\partial}{\partial x} = 0$ condition respectively.

In addition to resolving the flow in the slit, also the flow in the turbulent sub-channels needs to be resolved sufficiently. The grid spacing relative to the Kolmogorov scale η_K based on the average dissipation is equal to $\Delta = 4\eta_K$ for $Re_s \sim 10^4$, which is well below $15\eta_K$ as identified by Moin and Mahesh [21] as the scale *above* which most of the dissipation occurs. More critical is the resolution of the boundary layers in the turbulent sub-channels. The halfway bounce-back rule places grid nodes at a distance $\frac{\Delta}{2}$ from no-slip walls. At simulations with $Re_s \sim 10^4$, these near-wall points have $y^+ = \frac{u_w \Delta}{2\nu} \approx 2$. In direct simulations of channel flow it is usually recommended to take the first near-wall point within $y^+ \approx 1$ [22]. This condition has been relaxed somewhat here with a view to computational feasibility and also since we focus on the shear layers and their associated large-scale structures for which a slit-based Reynolds number may be more characteristic than the much higher Re_s. Still, the near-wall flow and the ability of the grid and the numerical method to adequately resolve turbulence will be further discussed in the subsequent section.

With a typical streamwise length of $L = 10.67D_h$, the number of lattice nodes for a simulation is 54 million. Such grids require 3.9 Gbyte of memory for flow only simulations. Scalar transport adds 0.9 Gbyte to this. The computer code was parallelized by dividing the flow domain in equal portions in the x-direction (subdomains). The lattice-Boltzmann method only requires communication of subdomain boundary values so that excellent parallel speed-up can be achieved, also when running on relatively low-end, PC-based hardware connected through fast Ethernet. For the above settings, the code is usually run on 12 CPU's in parallel so that less than 0.5 Gbyte of memory per CPU is required.

In order to quantify the level of cross-channel mixing, the transport equation

$$\frac{\partial c}{\partial t} + u \cdot \nabla c = \Gamma \nabla^2 c \tag{1}$$

for a passive scalar with concentration c and molecular diffusivity Γ was solved in conjunction with the flow field. The Schmidt number $Sc = \frac{\nu}{\Gamma}$ was set to a fixed value of 10^3 throughout this work. This value is representative for a weakly diffusing dye in liquid. For the system considered here it implies that scalar transport is dominated by convection. The velocity field u in Eq. (1) is the result of the lattice-Boltzmann simulation.

At the solid walls $\frac{\partial c}{\partial n} = 0$ is imposed as a boundary condition, with n the wall-normal direction. In order to assess how much scalar transfers from one sub-channel to the other, the scalar boundary conditions in streamwise direction are not periodic. At $x = 0$ in one sub-channel (the one with $y < -\frac{W}{2}$) a concentration $c = 1$ is maintained, the other sub-channel and the liquid in the slit are set to $c = 0$ there. In order to achieve a strong enough scalar flux in the other channel ($y > \frac{W}{2}$) so that mass transfer from one channel to the other can be estimated confidently the scalar passes twice through the periodic flow domain: If the scalar reaches $x = L$ it enters again at $x = 0$ and travels until $x = L$ (which in terms of the scalar now corresponds to $x = 2L$) where it leaves according to a $\frac{\partial c}{\partial x} = 0$ condition.

Eq. (1) is numerically solved with a finite volume scheme on the same uniform, cubic grid as used for the lattice-Boltzmann scheme. The finite volume scheme is explicitly stepped in time in an Adams–Bashford manner. Since the time step constraints (mainly related to limiting the compressibility of the lattice-Boltzmann liquid) are stricter for the lattice-Boltzmann than for the finite volume scheme the latter usually has bigger time steps ($\Delta t_{FV} = 2 \cdots 4\Delta t_{LB}$). An important issue when numerically solving transport equations with finite volume formulations is controlling numerical diffusion, specifically in the cases with high Schmidt numbers; numerical diffusion should not overwhelm molecular diffusion, and transport associated with numerical diffusion should certainly not become comparable to large-scale convective transport. As in

our previous works [23,24], TVD discretization with the superbee flux limiter for the convective fluxes [25,26] was employed.

The high value of the Schmidt number implies that the fine scalar scales are much smaller than the fine flow scales: $\eta_B = \eta_K Sc^{-1/2}$ with η_B and η_K the Batchelor and Kolmogorov scale respectively. With the current grids we in general do not resolve the Batchelor scale. However, we do resolve the macroscopic scalar distributions. This serves the purpose we have for the scalar transport computations: quantifying the levels of macroscopic, cross-channel transport.

4. Flow field results

4.1. Flow impressions

As the base-case we consider the flow simulation at Re_s = 9300 in an x-periodic domain with length $L = 10.67D_h$ at a resolution such that the gridspacing Δ of the uniform, cubic grid corresponds to $\Delta = \frac{d}{15}$. This case will be used to illustrate the basic flow features, to demonstrate the way the flow is analyzed in terms of structure speed and structure size, and to check the sensitivity of the simulation results with respect to numerical parameters and choices regarding boundary conditions.

In Fig. 3, various cross sections through the flow in terms of velocity vector fields are given for a single flow realization. The xy-cross section, halfway through the slit ($z = \frac{d}{2}$) has the meandering pattern characteristic for the cross flow phenomenon. The close proximity of walls makes the flow in the slit much slower than the flow in the sub-channels. The flow-normal (yz) cross section shows significant communication between the two sub-channels via the slit. This cross section also reveals the typical turbulent character of channel flows with turbulence being generated in the shear layers near the walls. The xz-cross section (at a distance of y^+ = 27 from a no-slip wall) shows the streaky patterns (low-speed streaks) characteristic of near-wall turbulence. As can also be observed, the cross flow adds to the turbulence: in the low-z part of the xz-cross section turbulent activity is significantly higher than in the rest of the sub-channel.

In what follows now, we focus on the large-scale flow structures in the xy-cross section at $z = \frac{d}{2}$. Experiments [5] showed that these structures are transported in the streamwise direction with a well-defined velocity. In Fig. 4 a time series are plotted of the y-velocity in the center of the slit at three different axial locations with spacing $\Delta x = 0.889D_h$. These three signals are clearly correlated. Their time lags can be quantified by determining cross correlation functions (Fig. 4b): $C(\tau) = \frac{\langle u_y(t)u_y(t+\tau)\rangle}{u_s^2}$. The spacing Δx divided by the peak positions of the cross correlation functions τ_d is the structure speed: $u_{struct} = \frac{\Delta x}{\tau_d}$. For this specific case we find u_{struct} = 0.709u_s. The experimental value [5] at roughly the same Reynolds number is 0.8u_s.

During the simulations, velocity information in the entire $z = \frac{d}{2}$ plane was stored at regular time intervals ($\Delta t_{store} = 0.118\frac{D_h}{u_s}$ for the base-case simulation). With this information the time-averaged shape of the large-scale flow structure in the $z = \frac{d}{2}$ plane has been determined by averaging the stored velocity fields, whereby first each field is shifted back in the x-direction according to the earlier determined structure velocity: The jth field is shifted over a negative x-distance of $(j-1)\Delta t_{store} u_{struct}$. A result of this conditional averaging is the velocity vector field as depicted in Fig. 5. It shows a coherent flow with four macroscopic structures fitting in the space between x = 0 and x = L. The fourfold periodicity of the flow is not perfect though. The second structure from the left is longer than the other three. The pattern as observed in Fig. 5 appeared insensitive to the length of the time-averaging window (as long as it was bigger than $\sim 25\frac{D_h}{u_s}$). Given the long averaging time used to determine Fig. 5 $\left(95\frac{D_h}{u_s}\right)$, we do not believe that the non-period-
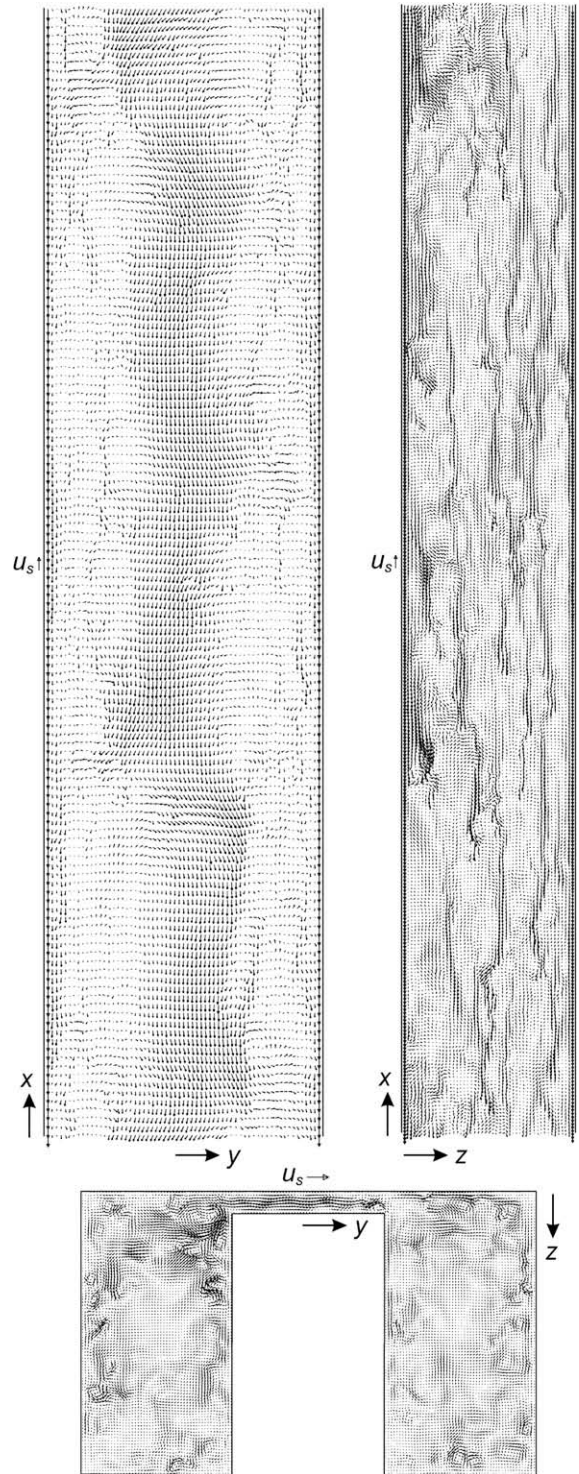

Fig. 3. Velocity vector plots in three cross sections through the flow for a single flow realization of the base-case. Top-left: xy-plane at $z = \frac{d}{2}$; in this plot the velocity vector $\mathbf{u} - u_s\mathbf{e_x}$ is drawn for every 10th node in x, and every 5th node in y-direction. Top-right: xz-plane for $y = -\frac{W}{2} - 0.06W$; $\mathbf{u} - u_s\mathbf{e_x}$ every 4th node in x and y-direction. Bottom: yz-plane at x = 0; every 2nd node in y and z-direction. The reference vectors per panel relate the vector *lengths* to u_s.

icity is a lack of statistical convergence; it more likely reflects the flow trying to select a structure size S different from L divided by an integer number. On average, the macro flow structure has a size $S = \frac{L}{4} = 2.67D_h$. At this Reynolds number ($\sim 10^4$) the experiments [5] report a size of 2.9D_h.
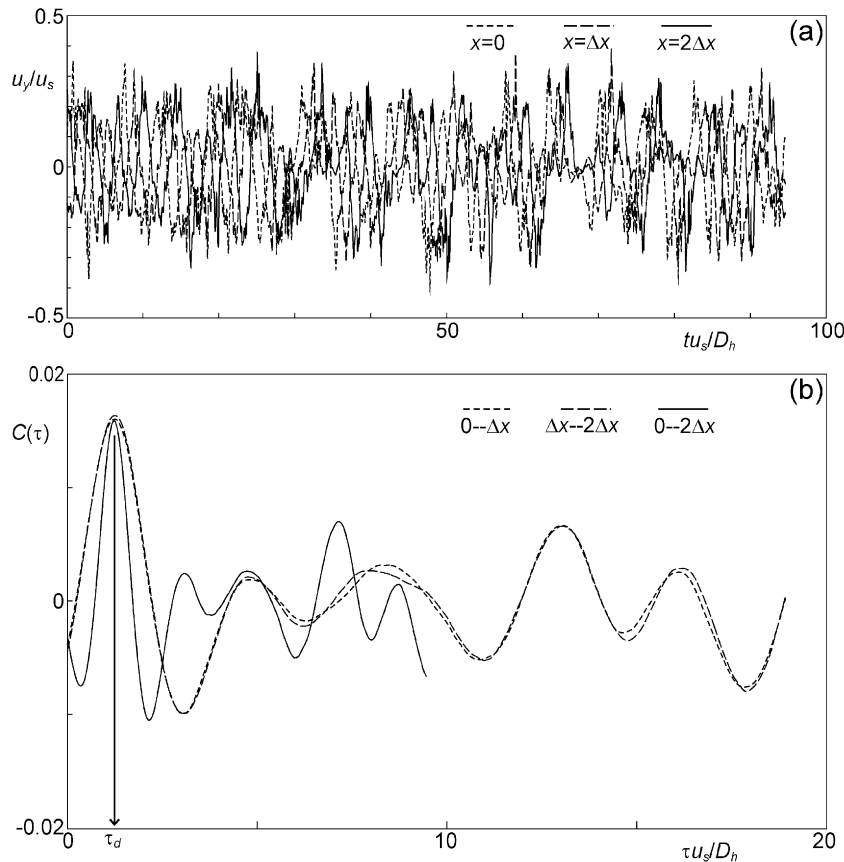
Fig. 4. (a) Time series of the transverse (y) velocity in the center of the slit at three axial locations ($x = 0$, $x = \Delta x$, $x = 2\Delta x$, with $\Delta x = 0.889 D_h$). (b) Cross-correlations of the three signals. Note that for the 0 to $-2\Delta x$ correlation function the time τ has been normalized with $\frac{2D_h}{u_s}$. Base-case simulation.
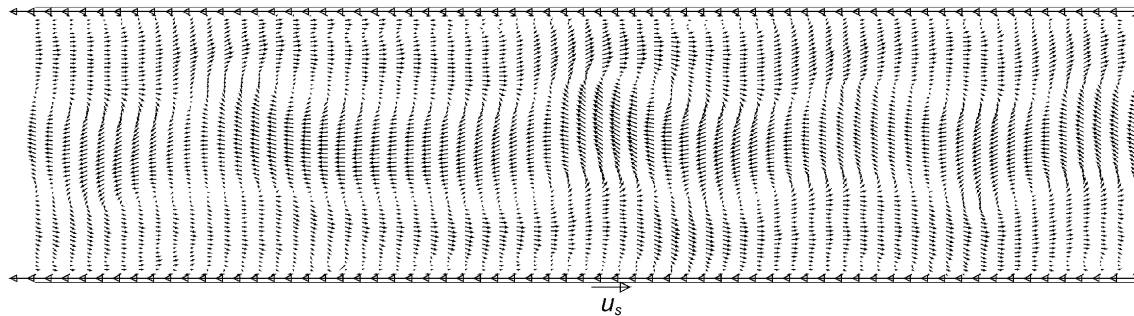

Fig. 5. Conditionally time-averaged velocity field in the $z = \frac{d}{2}$ plane. The flow was averaged over a time period of $95 \frac{D_h}{u_s}$. The vectors represent $u - u_{x,av} e_x$, with $u_{x,av}$ the average x-velocity in the plane under consideration. Base-case simulation.

4.2. Verifications

Before investigating to what extent the characteristics of the macroscopic structures depend on the Reynolds number Re_s, we first investigate the effects of numerical and other non-physical settings in the simulations: grid spacing, domain length, and boundary conditions in the x-direction.

Grid effects have been assessed by performing simulations at a Reynolds number close to the Reynolds number associated with the base-case at a higher $\left(\Delta = \frac{d}{20}\right)$ and at a lower $\left(\Delta = \frac{d}{10}\right)$ grid resolution. For computational reasons, the higher resolution simulation had a shorter domain length: $L = 3.56 D_h$ instead of $L = 10.67 D_h$. This forced the system to only contain one macroscopic flow structure which prohibits comparisons in terms of structure size and also structure speed. We did, however, compare the three resolutions in terms of the (unconditionally) aver-

aged streamwise velocity profile at $z = \frac{d}{2}$, see Fig. 6. If the number of grid spacings per slit height d is an even number (as with $\Delta = \frac{d}{20}$ and $\Delta = \frac{d}{10}$) flow information at $z = \frac{d}{2}$ was interpolated from the grid layers right above and below $z = \frac{d}{2}$. In Fig. 6 also experimental results are displayed. These results were obtained by [27] in the same flow rig, and with the same PIV setup as employed by [5]. The simulation results at different resolutions agree quite well. The experiment apparently had some trouble maintaining symmetry. The resemblance between the experimental and computational profiles is fairly good; the main deviations between experiment and simulation occur at the outer regions of the profiles, near the side walls. Lexmond et al. [5] have published an average velocity profile in the same xy-plane, however at a lower Reynolds number: $Re_s = 2690$. Again, this profile compares reasonably well with our simulation results at $Re_s = 2700$ (Fig. 7).
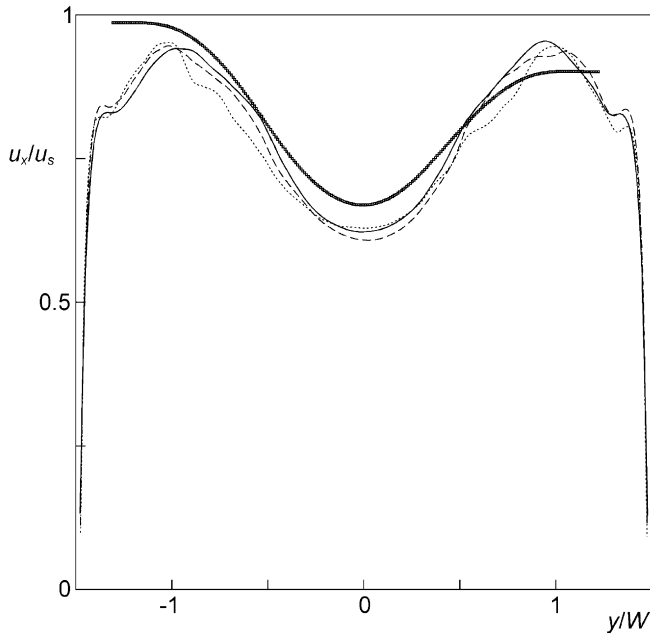
Fig. 6. Average streamwise velocity as a function of y at $z = \frac{d}{2}$. Closely spaced symbols: PIV experiments (Mahmood, 2008); dotted curve: simulation with $\Delta = \frac{d}{20}$; dashed curve: $\Delta = \frac{d}{15}$ (base-case); solid curve: $\Delta = \frac{d}{10}$.

Fig. 8. Axial velocity profile in wall units recorded at the positions as indicated in the schematic, that is halfway the two sub-channels, close to their lower walls. $y^+ = \frac{(H-z)u_w}{\nu}$, $u^+ \equiv \frac{u_x}{u_w}$. Square symbols: base-case simulation; plusses: lower resolution ($\Delta = \frac{d}{10}$); triangles: higher resolution ($\Delta = \frac{d}{20}$).

As mentioned above, resolution of the wall boundary layers in the base-case simulation requires careful consideration since the $y^+ \leqslant 1$ criterion for the nearest wall grid point is not met. In spite of this, the base-case simulation captures the viscous sublayer velocity profile $u^+ = y^+$, see Fig. 8. This figure displays the time and streamwise averaged axial velocity profile close to the lower wall of the sub-channels in terms of wall units (with $y^+ \equiv \frac{(H-z)u_w}{\nu}$ the dimensionless distance from the wall, and $u^+ \equiv \frac{u_x}{u_w}$). Fig. 8 also shows the effects of refining and coarsening the grid with an improved representation of the log-layer on the finer grid.

The turbulent nature of the flow under base-case conditions is further underlined by the one-dimensional wavenumber spectra
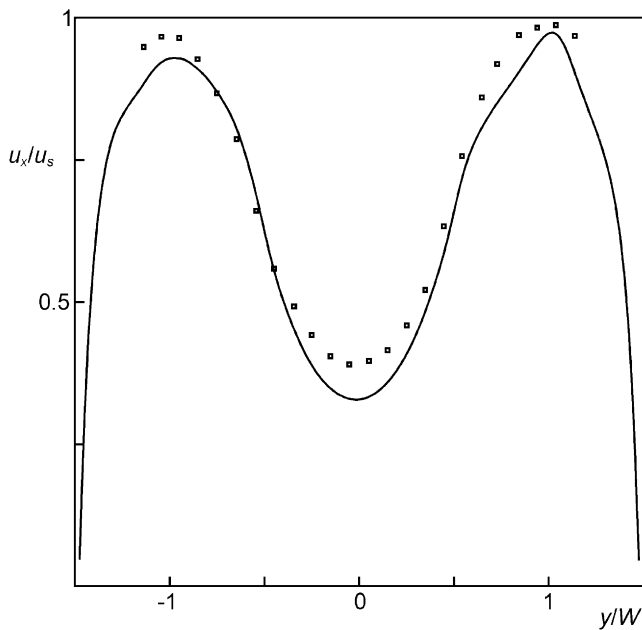
as given in Fig. 9 with $k_x^+ \equiv k_x \frac{\nu}{u_w}$ and $S_{ii}^+ \equiv \frac{\langle \tilde{u}_i \tilde{u}_i^* \rangle}{u_w^2}$ (the components i are streamwise (s), lateral (l). and wall-normal (n); $\tilde{u}_i(k_x)$ is the Fourier transform of $u_i(x)$; $*$ denotes the complex conjugate). The spectra show an inertial and a viscous range, and the usual distribution of the kinetic energy over the streamwise, lateral, and wall-normal directions which depends on the distance from the wall. They largely agree with simulated and measured near-wall turbulence spectra reported in the literature (e.g. [28]).

The base-case and low resolution case have also been compared in terms of structure velocity and size (Fig. 10). In terms of the strength and scale of the macroscopic structures the two simulations agree well. The structure velocity for the low resolution case was $u_{struct} = 0.747 v_s$, versus $0.709 u_s$ for the base-case. A minor portion of this difference can be explained by the fact that the Reynolds number of the coarser case is some 10% higher than the base-case Reynolds number; as we will see, the structure velocity increases with Re_s.

Fig. 7. Average streamwise velocity as a function of y at $z = \frac{d}{2}$. Symbols: PIV experiments (Lexmond et al., 2005) at $Re_s = 2690$; solid curve: simulations at $Re_s = 2700$ at a resolution $\Delta = \frac{d}{15}$.
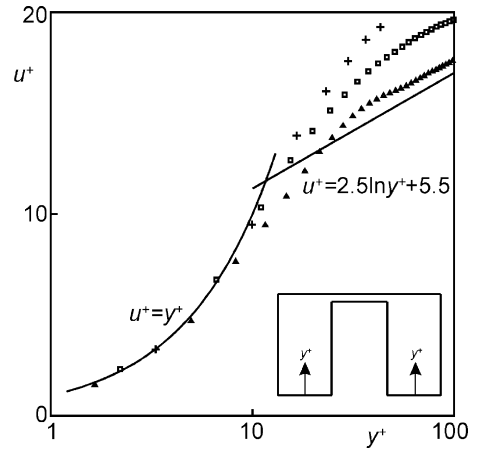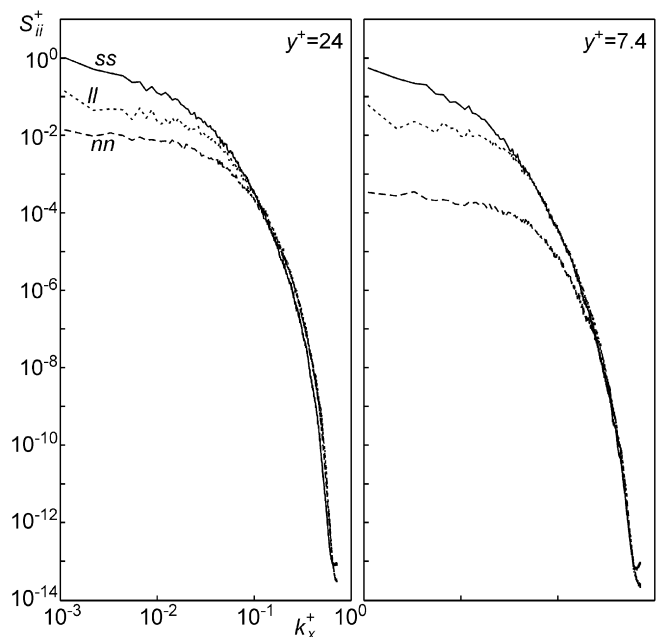

Fig. 9. One-dimensional spectra in wall units for the base-case simulation. The symbols k_x^+ and S_{ii}^+ are defined in the text.
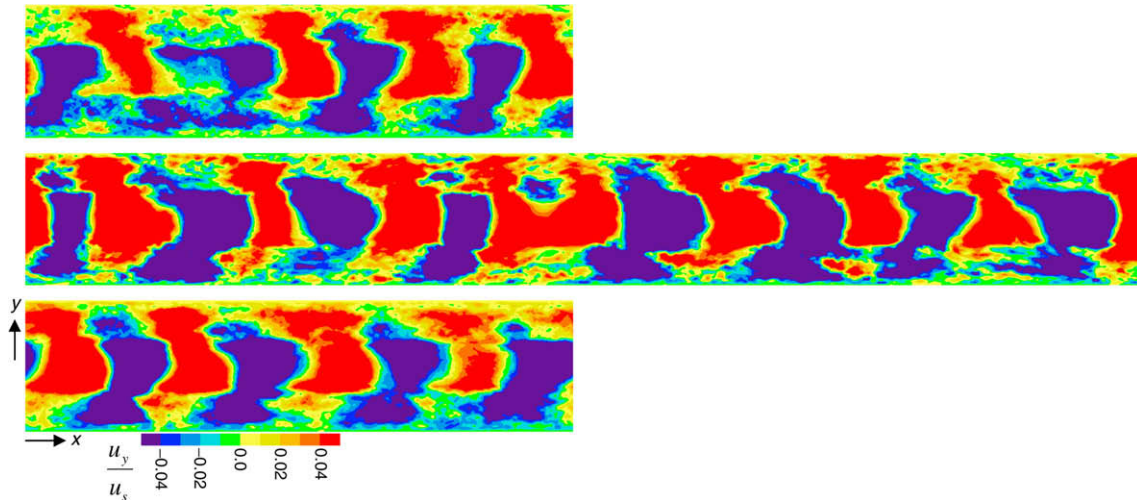
Fig. 10. Contours of conditionally averaged transverse (y) velocity in the $z = \frac{d}{2}$ plane for (from top to bottom) the base-case; a case with double the length of the base-case and for the rest the same conditions; a case with the same Re$_s$ as the base-case but with lower spatial resolution ($\Delta = \frac{d}{10}$ instead of $\Delta = \frac{d}{15}$).

Also in Fig. 10 is the result of a simulation with twice the length and the same resolution as the base-case. Now eight instead of four structures fit in the domain length, giving rise to the same (average) structure size. It should be noted that the double-length simulation was started from a zero-flow field, not from connecting two copies of the developed base-case field. The structures in the double-length simulation have a velocity of $0.706u_s$ which is very close to the base-case value.

So far we considered simulations with periodic boundary conditions in the streamwise (x) direction. Given that in an experiment it is quite impossible to create such conditions, and (more importantly) that periodic conditions in the present cases of (quasi) x-periodic flows lead to stepwise changes in the structure size S (only an integer number of structures fit in the periodic domain) the effect of the streamwise boundary conditions on the formation of large-scale flow structures has been checked. For this a simulation with the same spatial resolution as the base-case $\left(\Delta = \frac{d}{15}\right)$ was set up. At the inlet a uniform velocity u_{in} was imposed (so that the superficial velocity $u_s = u_{in}$), and at the exit $\frac{\partial}{\partial x} = 0$ for all variables. The case had Re$_s = \frac{u_s D_h}{\nu} = 9200$. In order to give this system the chance to develop macroscopic instabilities a domain length of $L = 29.6D_h$ was chosen. Cross flow instabilities akin to the ones observed with periodic boundary conditions indeed developed, see Fig. 11. This contour plot illustrates the onset of instabilities at the shear planes $\left(y = \pm\frac{W}{2}\right)$, starting at $x \approx 8.5D_h$, and getting fully developed at a distance $x \approx 20D_h$ from the inlet. This fully developed portion can be directly compared with the x-periodic base-case. In a qualitative sense this is done in Fig. 11 by showing a snapshot of the base-case flow at the same color and length scale as the non-periodic simulation. Both cases indeed have similar large-scale structure sizes.
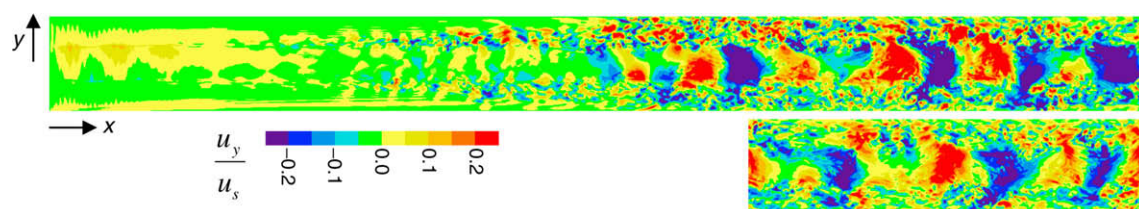
The non-periodic simulation does not directly allow for an analysis of the structure size by conditional averaging of x-shifted velocity fields as done for the periodic cases. It does allow, however, for a time-correlation analysis to determine the structure velocity. Fig. 12 shows cross correlation functions of time series in the fully developed flow region, from which a structure velocity $u_{struct} = 0.685u_s$ can be derived. This agrees quite well with the structure velocity of the base-case ($0.709u_s$). The correlation function is less pronounced than the one related to the base-case (Fig. 4b) indicating less coherent flow.

The above results demonstrate the feasibility of periodic boundary conditions to mimic the main cross flow characteristics, and also the (computational) reason for applying them: they prevent us from spending much computational effort in simulating the onset of instabilities. Roughly 2/3 of the domain as shown in Fig. 11 (top panel) is used for this. Also the level of grid sensitivity has been assessed, showing that $\Delta = \frac{d}{15}$ is an acceptable resolution for capturing the flow's essentials in the slit and the shear layers as well as the turbulence in the sub-channels.

4.3. Reynolds number effects

In addition to the base-case (Re$_s = 9300$), the flow system with periodic boundary conditions, a domain length of $L = 10.67D_h$, and a resolution such that $\Delta = \frac{d}{15}$ has been simulated for seven additional Reynolds numbers (Re$_s = 18,800, 12,700, 4900, 2700, 1550, 1360$ and 980).

At the three highest Reynolds numbers spatial resolution limitations are definitely at issue, specifically related to the boundary layers in the sub-channels. Turbulence spectra at Re$_s = 18,800$, however, show that the grid recovers the dissipation range (Fig. 13) and hint at physically sound turbulence at the highest
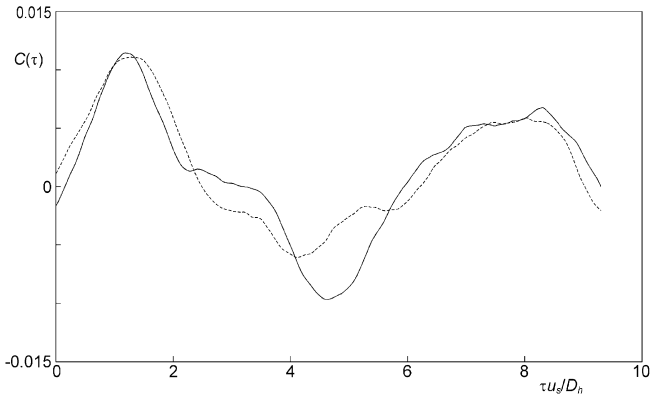

Fig. 11. Single realizations of the transverse (y) velocities in the plane $z = \frac{d}{2}$ for the case with uniform inlet velocity and zero-gradient outlet (top), and for the (x-periodic) base-case (bottom).

Fig. 12. Cross correlation functions of the transverse velocity in the center of the slit of the points at $x = 26.34D_h$ and $x = 27.16D_h$ (dashed line), and the points at $x = 27.16D_h$ and $x = 27.98D_h$ (solid line) for the case with uniform inlet velocity and zero-gradient outlet.

Reynolds number considered here. Comparison with the spectra at $Re_s = 9300$ (Fig. 9) reveal a slight widening of the wavenumber range as Re_s increases.

In terms of the large-scale flow structures, the main Reynolds number effect is the reduction of the strength and the coherence of the cross flow when the Reynolds number is reduced, see Fig. 14. This figure shows the conditionally averaged (shifted) flow at different Reynolds numbers. At $Re_s = 980$ cross flow is absent, as also illustrated in Fig. 14. These results are in qualitative agreement with the experiments [5] that saw a weakening of structure strength and a steep increase in structure size if Re_s approaches 1400, coming from higher values. In the range $2000 < Re_s < 10,000$ the structure size in the experiments is independent of Re_s in agreement with the simulations, albeit that in the latter the structure size is quantized, i.e. gradual changes are not possible. The velocity with which the large-scale structures are advected decreases relative to the superficial velocity with decreasing Reynolds number (Fig. 15, top panel). In the same figure it is also indicated how the Reynolds number based on the wall shear velocity (Re_w) relates to Re_s.

Fig. 13. One-dimensional spectra in wall units for $Re_s = 18,800$. The resolution is such that $\Delta = \frac{d}{15}$.
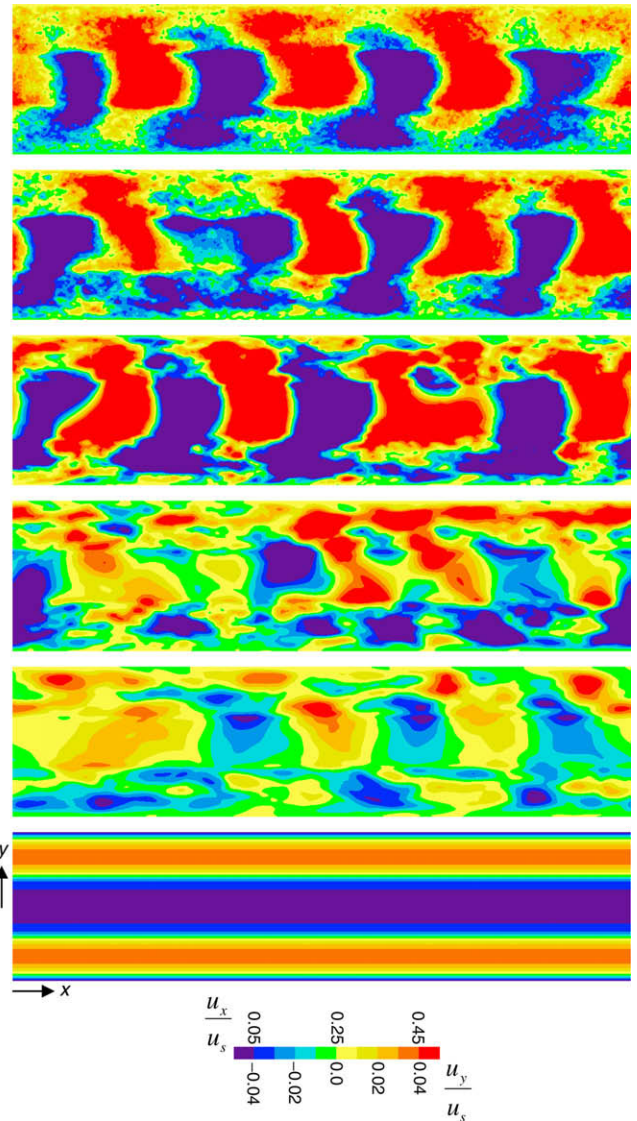

Fig. 14. Average velocity contour plots in the $z = \frac{d}{2}$ plane at various Reynolds numbers. Top four panels: conditionally averaged transverse (y) velocity at $Re_s = 18,800$, 9300, 4900, 2700, and 1550 (top to bottom). Bottom panel: average streamwise (x) velocity at $Re_s = 980$.
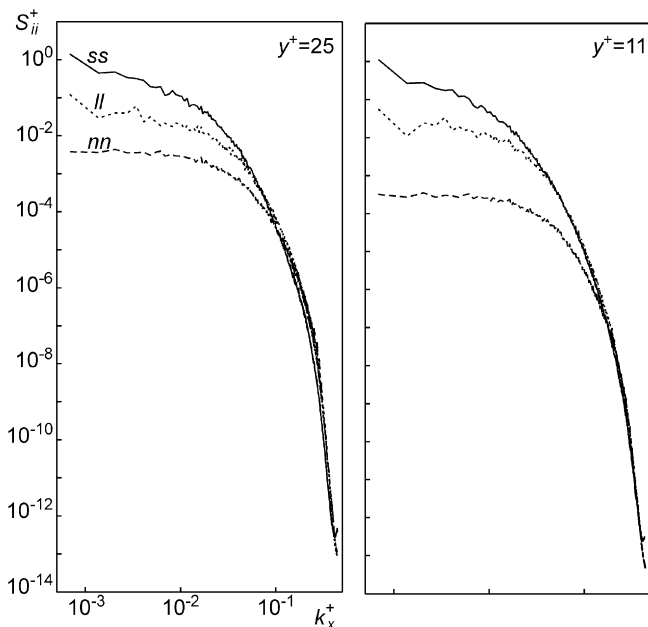
The onset of the cross flow instability is illustrated in Fig. 16. Here we show a time series of the transverse velocity in the center of the slit. The starting point ($t = 0$) is the (stable) solution at $Re_s = 980$. At $t = 0$ the kinematic viscosity is reduced by a factor 0.625, and the simulation is continued with that new viscosity. The flow quickly develops cross flow in the slit with an amplitude that increases in time. At $\frac{tu_s}{D_h} \approx 200$, however, the periodicity breaks down and the signal gets incoherent. As can be seen from the single flow realizations in Fig. 16, at that stage the cross flow triggers a transition from laminar to mildly turbulent flow in the two sub-channels. This transition feeds back to the cross flow in the slit leading to less coherent cross flow. After $\frac{tu_s}{D_h} \approx 200$ the flow rate stabilized at a level such that $Re_s = 1550$.

We did not succeed in reaching a stable periodic state – i.e. a state with cross flow having constant amplitude in the slit and laminar flow in the sub-channels. For instance, at $Re_s = 1360$ the flow turned steady with zero transverse velocity (much like the flow at $Re_s = 980$) and stayed so for a period of $\frac{D_h}{u_s} = 45$ after which the simulation was aborted.
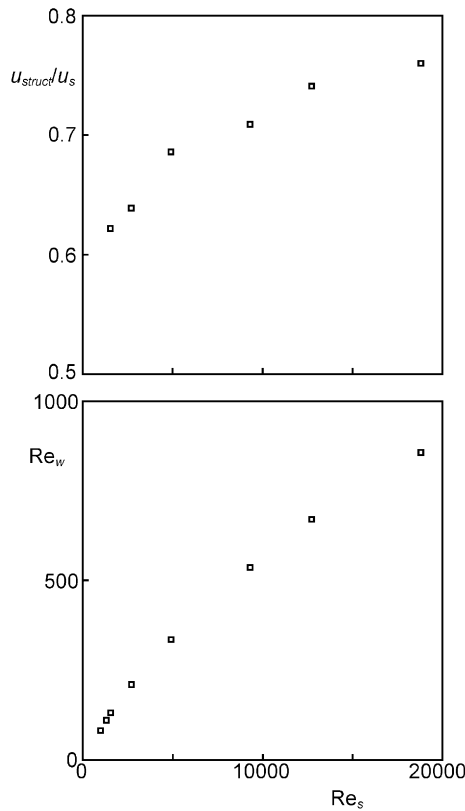
Fig. 15. Structure velocity relative to superficial velocity versus Re_s (top panel), and the Reynolds number based on the wall shear velocity Re_w versus Re_s (bottom panel).

5. Scalar transport results

Once the flow is fully developed, a passive scalar is injected in the sub-channel with $y < -\frac{W}{2}$: at $x = 0$ a scalar concentration $c = 1$ is maintained in the entire cross section of this sub-channel. What subsequently happens in the plane with $z = \frac{d}{2}$ is shown in Fig. 17: the scalar gets advected by the turbulent flow and spreads in streamwise and lateral direction, the latter due to cross flow. In Fig. 17 the domain has length $2L$. As explained above, the flow field in the range $L < x < 2L$ is a copy of the one with $0 < x < L$. Scalar leaving at $x = L$, however, reenters at $x = 0$ and makes a second run through the same flow field before it really leaves. At that stage, part of the scalar has made its way to the other sub-channel (with $y > \frac{W}{2}$) as can be seen in the yz-cross section in Fig. 18 (note the difference in color scale between Figs. 17 and 18). Mass transfer between the two sub-channels has been quantified by equating the amount of scalar transported in one channel with the amount transported in the other.

Quasi steady state in terms of the scalar field in the entire channel is reached when $t > 40\frac{D_h}{u_s}$ after the moment scalar injection was started. After the start-up phase we see that the scalar flow rate through the sub-channel with $y > \frac{W}{2}$ (symbol $\phi_{y>W/2}$) is highly intermittent: the cross flow through the slit intermittently drives scalar into, and extracts scalar from the channel with $y > \frac{W}{2}$ (Fig. 19). The time-averaged scalar concentration taken over a period $56\frac{D_h}{u_s}$ beyond $t = 40\frac{D_h}{u_s}$ is given in Fig. 20, and shows lateral spreading.

The time-averaged, lateral scalar transfer flux through the slit between the two sub-channels can be characterized with an average mass transfer coefficient k: $\langle\phi_L''\rangle = k\Delta c$ with $\langle\phi_L''\rangle$ the average scalar flux in lateral direction through the slit, and Δc the macroscopic concentration difference between the two sub-channels (Δc is virtually constant and equal to 1 given the small amount of scalar being cross-transferred over the limited length of the channel). In the above terms, the rate with which the scalar is transported by the $y > \frac{W}{2}$ sub-channel in the streamwise direction should increase linearly with x: $\langle\phi_{y>W/2}\rangle = \int_{x_0}^{x} kd\Delta c dx = k(x - x_0) d\Delta c$ (with the slit height d in the role of mass exchange surface per unit length, and x_0 the axial location where scalar starts entering the $y > \frac{W}{2}$ sub-channel). Given the on average uniform flow conditions in x-direction, k is independent of x. The linear increase of $\langle\phi_{y>W/2}\rangle$ with x is actually observed, see Fig. 21. The mass transfer coefficient k then follows from the slope of a straight line fitted through the points in Fig. 21.
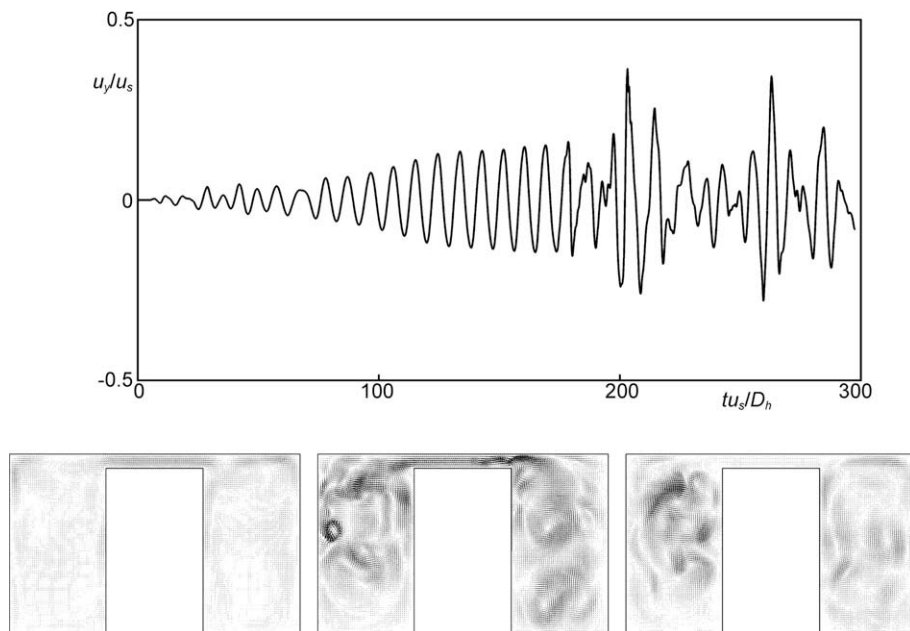

Fig. 16. Top: time series of the transverse (y) velocity in the center of the slit starting from a steady state solution at $Re_s = 980$. The flow evolves towards $Re_s = 1550$. Bottom: snapshots of the flow in yz-cross sections in terms of velocity vectors at (from left to right) $\frac{tu_s}{D_h} = 134$, 197, and 298.
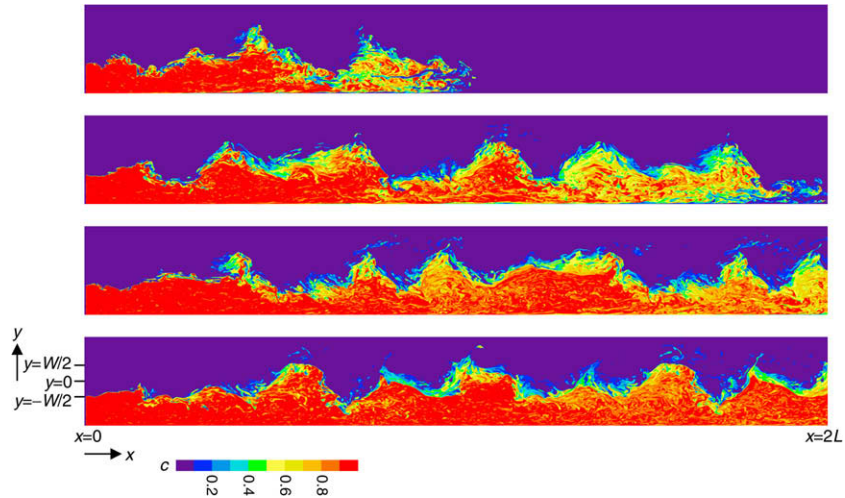
Fig. 17. Scalar concentration in the $z = \frac{d}{2}$ plane at four moments after starting its release in fully developed flow at $x = 0$ in the sub-channel with negative y. From top to bottom: $\frac{tu_s}{D_h}$ = 9.30, 18.6, 27.9, 37.1. Base-case.
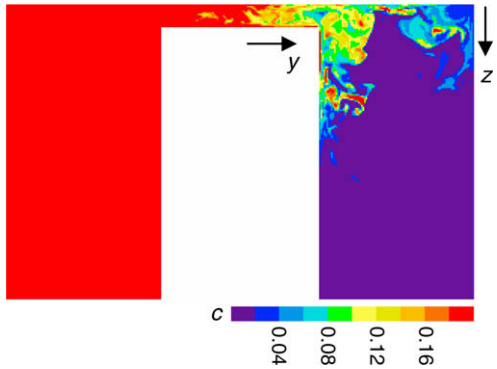

Fig. 18. Instantaneous realization of the scalar concentration in the $x = 1.92L = 20.5D_h$ plane after quasi steady scalar transport conditions have been reached. Base-case.

The flow cases at the other Reynolds numbers have also been analyzed in the above manner, and mass transfer coefficients have been determined (see Fig. 22). As can be anticipated, the non-dimensional mass transfer coefficient $\frac{k}{u_s}$ depends on the Reynolds number. Our observations of a weakening cross flow with decreasing Reynolds number are reflected here: the lower the Reynolds number, the weaker the cross flow and thus the lower k. The relatively large uncertainty of the first two non-zero data points is due to the very limited amount of scalar that makes its way across the slit over the length $2L$ making the estimate of the $\langle \phi_{y>W/2} \rangle$ versus x slope uncertain. The three points with the highest Reynolds numbers have approximately – within a 10% range – the same non-dimensional mass transfer coefficients. In the absence if cross flow (i.e. at $Re_s \leqslant 1360$) the only transfer mechanism is molecular diffusion which is marginal.
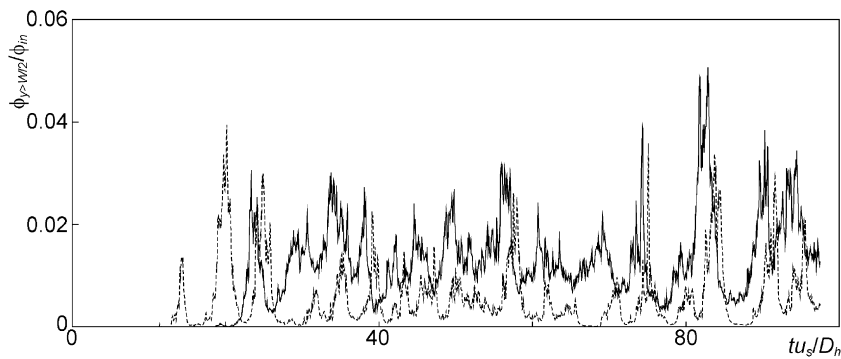

Fig. 19. Scalar flux in the sub-channel with $y > \frac{W}{2}$ at $x = L$ (dashed curve), and $x = 1.92L$ (solid curve) as a function of time. Base-case.
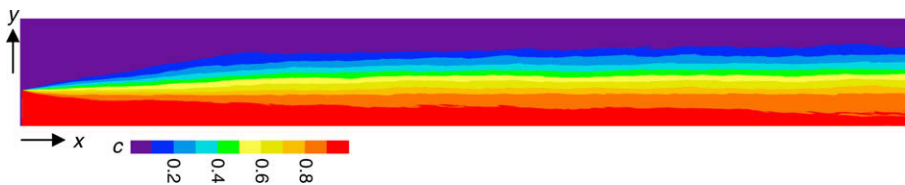

Fig. 20. Time-averaged (averaging window $40 < \frac{tu_s}{D_h} < 96$) scalar concentration in the plane $z = \frac{d}{2}$. Base-case.
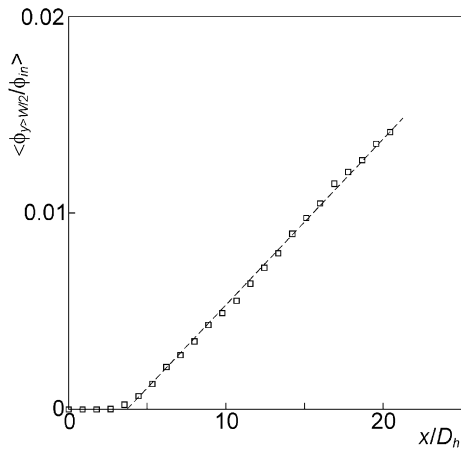
Fig. 21. Time-averaged scalar flux in the sub-channel with $y > \frac{W}{2}$ as a function of x under quasi steady conditions. The straight, dashed line is a least-squares fit through the points with $\frac{x}{D_h} > 5$. Base-case.
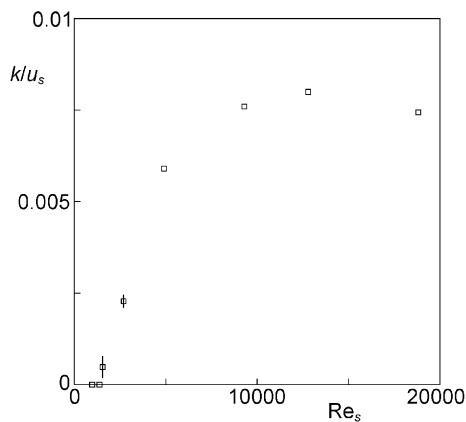

Fig. 22. Mass-transfer coefficient as a function of Re_s. Where no error bars are given the uncertainty is comparable to the size of the symbol.

6. Summary

Numerical simulations of the laminar, transitional and turbulent flow in a long channel with uniform cross section have been performed. The cross section consists of two sub-channels connected by a narrow slit. The single phase flows considered were isothermal and incompressible. For discretizing the Navier–Stokes equations the lattice-Boltzmann method [14] was used. No turbulence modelling was used. The focus of the study was on the onset of flow instabilities, their characteristic size and velocity, and the level of cross flow and related mass transfer between the sub-channels.

The cross flow is due to instabilities that develop at the free shear layers at the interfaces between the sub-channels and the slit. We observed the onset of the instabilities at a Reynolds numbers (based on macroscopic flow quantities) of 1550. They generate a meandering flow pattern in the slit. At the latter Reynolds number, the cross flow triggers a transition to turbulence in the two sub-channels. At higher Reynolds numbers (Re > 9000), the transverse velocities are of the order of 0.1 times the streamwise superficial velocity in the channel.

The numerical procedure for performing the simulations has been verified and assessed by comparing its results with experimental data from the literature, and by checking grid effects; the three-dimensional grid has been refined/coarsened such that the finest and coarsest grids differed by a factor of two in linear spac-

ing. Fairly good agreement between simulations and experiment was achieved in terms of average streamwise velocity profiles, with the numerical results largely insensitive to the grid resolution. Also the velocity with which the cross flow structures were advected, and their size agreed reasonably well with the experimental data. Turbulence spectra derived from the flow in the sub-channels showed resolution up to the viscous wavenumber range. Boundary layers in the sub-channels were well resolved with the finest grid. With the default grid (that has a 33% larger grid spacing compared to the finest grid) deviations of up to 10% in the logarithmic wall layer were observed.

For computational reasons, most of the simulations were carried out in domains with periodic conditions in streamwise direction. This allows for only an integer amount of structures in the domain. It was, however, verified that the size (length) of the structures was independent of the length of the computational domain, and that structures with similar properties also develop if non-periodic boundary conditions were applied.

With the motivation of the research in mind (heat transfer in tube bundles), the flow simulations have been directly coupled with the transport of a passive scalar. Its transport equation was solved by means of a finite volume solver on the same grid as used by the lattice-Boltzmann method. The cross flow transfers the scalar between the two sub-channels in a highly intermittent way. From the scalar transport calculations mass transfer coefficients have been derived that describe the level of time-averaged interaction between the sub-channels. With the strength of the cross flow, mass transfer increases with Re. At the high end of the Reynolds number range considered here ($9300 < Re_s < 18{,}800$) the mass transfer coefficient is 0.0076 (± 0.0003) times the superficial velocity.

A goal for further research is to systematically study the effects of the channel geometry on the level of cross mass transfer with a view to e.g. process or equipment optimization. From a practical and also scientific point of view, a very interesting challenge is to extend the present simulation procedure to multiphase (gas–liquid) flow in order to describe the heat and mass transfer in boiling systems. This could go along the lines of two-fluid modelling, preferably without inferring turbulence modelling, i.e. directly solving the dynamic equations for two interpenetrating continua. In a lattice-Boltzmann context, interesting progress has recently been reported in [29].

References

[1] Rowe DS, Johnson BM, Knudsen JG. Implications concerning rod bundle crossflow mixing based on measurements of turbulent flow structures. Int J Heat Mass Trans 1974;17:407–19.
[2] Meyer L, Rehme K. Large-scale turbulence phenomena in compound rectangular channels. Exp Therm Fluid Sci 1994;8:286–304.
[3] Barsamian HR, Hassan YA. Large eddy simulation of turbulent cross flow in tube bundles. Nucl Eng Des 1997;172:103–22.
[4] Möller SV. Single-phase turbulent mixing in rod bundles. Exp Therm Fluid Sci 1992;5:26–33.
[5] Lexmond AS, Mudde RF, Van der Hagen THJJ. Visualisation of the vortex street and characterization of the cross flow in the gap between two sub-channels. In: Proceedings of the 11th international topical meeting on nuclear reactor thermal-hydraulics (Avignon, France) paper #122; 2005. 19p.
[6] Brown GL, Roshko A. Density effects and large structure in turbulent mixing layers. J Fluid Mech 1974;64:775–816.
[7] Ho CM, Huerre P. Perturbed free shear layers. Ann Rev Fluid Mech 1984;16:365–424.
[8] Cortesi AB, Smith BL, Yadigaroglu G, Banerjee S. Numerical investigation of the entrainment and mixing processes in neutral and stably-stratified mixing layers. Phys Fluids 1999;11:162–85.
[9] Balaras E, Piomelli U, Wallace JM. Self-similar states in turbulent mixing layers. J Fluid Mech 2001;446:1–24.
[10] Narayanan C, Lakehal D. Particle transport and flow modification in planar temporally evolving laminar mixing layers, I. Particle transport under one-way coupling. Phys Fluids 2006;18:093302.
[11] Ko J, Lucor D, Sagaut P. Sensitivity of two-dimensional spatially developing mixing layers with respect to uncertain inflow conditions. Phys Fluids 2008;20:077102.

[12] Wei M, Rowley CW. Low-dimensional models of a temporally evolving free shear layer. J Fluid Mech 2009;618:113–34.

[13] Chen S, Doolen GD. Lattice-Boltzmann method for fluid flows. Annu Rev Fluid Mech 1998;30:329–64.

[14] Succi S. The lattice Boltzmann equation for fluid dynamics and beyond. Oxford: Clarondon Press; 2001.

[15] Somers JA. Direct simulation of fluid flow with cellular automata and the lattice-Boltzmann equation. Appl Sci Res 1993;51:127–33.

[16] Eggels JGM, Somers JA. Numerical simulation of free convective flow using the lattice-Boltzmann scheme. Int J Heat Fluid Flow 1995;16:357–64.

[17] Qian YH, d'Humieres D, Lallemand P. Lattice BGK for the Navier–Stokes equations. Europhys Lett 1992;17:479–84.

[18] Eggels JGM. Direct and large-eddy simulations of turbulent fluid flow using the lattice-Boltzmann scheme. Int J Heat Fluid Flow 1996;17:307–23.

[19] Derksen J, Van den Akker HEA. Large-eddy simulations on the flow driven by a Rushton turbine. AIChE J 1999;45:209–21.

[20] Derksen JJ. Simulations of confined turbulent vortex flow. Comput Fluids 2005;34:301–18.

[21] Moin P, Mahesh K. Direct numerical simulation: a tool in turbulence research. Annu Rev Fluid Mech 1998;30:539–78.

[22] Li Y, McLaughlin JB, Kontomaris K, Portela L. Numerical simulation of particle-laden channel flow. Phys Fluids 2001;13:2957–67.

[23] Hartmann H, Derksen JJ, Van den Akker HEA. Mixing times in a turbulent stirred tank by means of LES. AIChE J 2006;52:3696–706.

[24] Derksen JJ. Scalar mixing by granular particles. AIChE J 2008;54:1741–7.

[25] Harten A. High resolution schemes for hyperbolic conservation laws. J Comput Phys 1983;49:357–64.

[26] Sweby PK. High resolution schemes using flux limiters for hyperbolic conservation laws. SIAM J Numer Anal 1984;21:995–1011.

[27] Mahmood M. Personal communication. The Netherlands: Delft University of Technology; 2008.

[28] Eggels JGM, Unger F, Weiss MH, Westerweel J, Adrian RJ, Friedrich R, et al. Fully developed turbulent pipe flow: comparison between direct numerical simulation and experiment. J Fluid Mech 1994;268:175–209.

[29] Sankaranarayanan K, Sundaresan S. Lattice Boltzmann simulation of two-fluid model equations. Ind Eng Chem Res 2008;47:9165–73.